Sensors & Actuators: A. Physical 379 (2024) 115941

Contents lists available at ScienceDirect

Sensors and Actuators: A. Physical

journal homepage: www.journals.elsevier.com/sensors-and-actuators-a-physical

An electromagnetic indirect-driving scanning mirror for wide-field coaxial LiDAR applications

Shuangliang Li [a], Di Wang [b], Dezhen Song [b], Jun Zou [a,*]

[a] Department of Electrical and Computer Engineering, Texas A&M University, College Station, TX 77843, USA
[b] Department of Computer Science and Engineering, Texas A&M University, College Station, TX 77843, USA

ARTICLE INFO

Keywords:
Micro scanning mirrors
LiDAR
Mechanical coupling
Indirect driving
Scan position sensing

ABSTRACT

This paper reports an electromagnetic indirect-driving scanning mirror with an enlarged mirror plate (***17mm*** × ***17mm***) supported by high-strength polymer hinges for wide-field coaxial LiDAR (Light Detection and Ranging) applications. An indirect-driving mechanism was developed to achieve large tilting angle through mechanical amplification, while maintaining a relatively high resonance frequency of the enlarged mirror plate. A prototype mirror was designed, fabricated, and tested. A Hall scan position sensor was integrated to monitor the pose of the mirror in real time. The testing results show a coupled resonance frequency of 54.9 ***Hz*** with an optical tilting angle of ±***60***°, corresponding to a field of view (FoV) of 12***0***°. A wide-field coaxial LiDAR system was also built based on the indirect-driving scanning mirror, and 2D imaging was demonstrated.

1. Introduction

Significant advancements have been achieved in the field of autonomous driving with the recent development and utilization of the scanning LiDAR. Based on the optical beam steering mechanisms, current scanning LiDAR technologies can be divided into three main categories: optical phased arrays (OPAs) [1–3], rotational motors [4–6], and MEMS (microelectromechanical systems) scanning mirrors [7–10]. The MEMS mirror-based scanning LiDAR has high scanning speed, low power consumption, small factor, and light weight, which is especially suitable for unmanned mobile platforms with limited power supply and payload capacity. Due to the small mirror plate size (e.g., ∼ mm^2) [11,12], MEMS mirror-based scanning LiDARs usually adopts a non-coaxial optical design, where light transmitting and receiving are along two different paths. As shown in Fig. 1(a), the scanning mirror steers the (collimated) transmitting light beam, while the reflected or back scattered light from the target is collected by a static receiver at an offset position. However, with the existence of ambient light interference, the reception sensitivity and field of view (FoV) of the optical receiver have to be balanced to ensure acceptable signal-to-noise ratio (SNR) [5,11,13]. This limitation can be lifted by using a coaxial design with increased receiving aperture, where light transmitting and receiving follow the same path and co-steered by the scanning mirror (Fig. 1(b)). In order to provide larger receiving aperture and sensitivity and also enable multi-beam scanning capability, a much larger (e.g., ∼ cm^2) mirror plate would be needed, which otherwise could pose challenges in the design and fabrication of the MEMS scanning mirror and also limit its scanning performance. For example, current MEMS scanning mirrors use torsional silicon hinges, which would be too brittle or fragile to support centimeter-sized mirror plates. Previously, flexible polymer or elastomer materials were used to form torsional or bending hinges for centimeter-sized mirror plates due to their large ultimate strain and impact resistance [14–17]. Nevertheless, with low Young's modulus, the polymer or elastomer hinges have to be made relatively short and thick to provide enough force constants for achieving desirable resonance frequencies. Because of this, the internal stress inside the hinges will increase fast with the tilting angle [17]. To avoid permanent degradation or damage, the maximal tilting angle (FoV) will have to be reduced. This situation forms a tradeoff between the scanning frequency and FoV, which is undesirable for LiDAR applications where both high scanning frequency and wide FoV are required. Although there were some previous efforts to achieve both high scanning frequency and wide FoV for MEMS scanning mirrors [18–21], these designs are still limited to relatively small (mm^2) mirror plates, which are insufficient for coaxial LiDAR applications.

This paper reports a new electromagnetic indirect-driving scanning mirror for coaxial LiDAR designs. The scanning mirror consists of an enlarged mirror plate (17mm × 17mm) supported by two torsional

* Corresponding author.
E-mail address: junzou@tamu.edu (J. Zou).

https://doi.org/10.1016/j.sna.2024.115941
Received 19 June 2024; Received in revised form 21 September 2024; Accepted 30 September 2024
Available online 7 October 2024

hinges made of high-strength polymers with good impact resistance. The utilization of the indirect-driving mechanism allows the use of softer hinges to achieve a larger torsion angle without sacrificing the resonance frequency. To precisely monitor the position of the mirror plate, a Hall scan position sensor is also built into the scanning mirror. For the demonstration, a prototype scanning mirror was designed, fabricated, and characterized. An experimental coaxial LiDAR setup was also built with the fabricated scanning mirror to evaluate its feasibility and imaging capability.

2. Design

Fig. 2 shows the schematic designs of the electromagnetic direct- and indirect- driving scanning mirrors. As shown in Fig. 2(a), the direct-driving scanning mirror consists of a mirror plate, which is supported on an outer frame by one pair of torsion hinges. Two permanent driving magnets (DMs) (having opposite polarity) are directly attached onto the mirror plate, which forms a part of the electromagnetic actuator (consisting of an inductor coil and the two magnets). When a DC or AC current flows through the inductor coil, a magnetic torque will be generated to tilt the mirror plate around the two torsion hinges. While the direct-driving design is compact, the addition of the two DMs can significantly increase the overall mass of the mirror plate. Fig. 2(b) shows the indirect-driving scanning mirror design, which consists of a mirror plate (the same scale as the mirror plate in Fig. 2(a)), an inner frame and an outer frame linked to each other with two pairs of torsion hinges. The outer frame is fixed onto the base, which is also the holder of the driving inductor coils. Two groups of DMs (red part represents the north while white part represents the south) are attached onto the inner frame around its center axis. They form two individual electromagnetic actuators with the inductor coils underneath. When AC currents flow into the inductor coils, an alternating magnetic force will be generated onto the DMs to tilt the inner frame around its central axis back and forth (Fig. 2(c)). The dotted line represents the inner frame, also showing the DMs in two states of tilting. By matching their resonance frequencies, the small titling angle (β) of the electromagnetic actuator is amplified into a much larger tilting angle (α) of the mirror plate. This mechanical amplification mechanism has been demonstrated in works [22–25]. Without the additional mass added to the mirror plate, a relatively high resonance frequency can be achieved even with softer hinges that can withstand larger torsion angle without permanent degradation or damage. In the current design, BoPET (biaxially oriented polyethylene terephthalate) is used as the material for the inner torsion hinges while acrylic is used as the materials for the outer torsion hinges and frame, due to their high mechanical strength and moderate Young's modulus of several *GPa*.

For resonant scanning mirrors, there is always a time delay between the driving signal and the mirror tilting angle. Therefore, the actual pose of the mirror plate cannot be deduced directly from the phase of the driving signal, which calls for in-situ scan position sensing. Traditional capacitive and piezoresistive sensing are difficult to implement on the non-conducting polymer hinges [26,27]. Optical position sensing is complex and oftentimes suffers from non-linearity and limited range [28]. Magnetic noncontact sensing based on a static Hall element and moving sensing magnets (mounted on the mirror plate) would be the best choice (Fig. 2(d)). With the indirect-driving mechanism, the driving magnets and coils are located far away from the mirror plate, and therefore the electromagnetic interference to the Hall scan position sensor can be minimized. Table 1 lists the material properties and main design parameters of the indirect-driving scanning mirror (with a targeted resonance frequency of 50 *Hz*).

3. Simulation

A finite element simulation was conducted with COMSOL Multiphysics® to determine the resonance frequencies of the mirror plate and the inner frame, and to estimate the torsional force constants of both hinges. The simulation model consisted of the entire upper mirror structure except the driving coils and holder. The surrounding medium was designated as air to represent the actual working environment. The simulated isolated eigen-frequencies of the mirror plate and the inner frame were 56.1*Hz* and 65.7*Hz*, respectively. To determine the torsional force constant of the inner hinges, a 0.001*N* normal load was applied onto the mirror plate when the inner and outer frames were both fixed. The resulting displacement of the two sides of the mirror plate was calculated as $1.6 \times 10^{-5} m$ (Fig. 3(a)). Similarly, to determine the torsional force constant of the outer hinges, a 0.1*N* normal load was applied on the inner frame when the outer frame was fixed. The resulting displacement of the two sides of the inner frame was calculated as $1.9 \times 10^{-4} m$ (Fig. 3(b)). The torsional force constants of the inner hinges and the outer hinges were calculated by

$$k = \frac{F \bullet d}{4 \bullet \arcsin(\frac{D}{w})} \tag{1}$$

where k is the torsional force constant of a single hinge, F is the applied force, d is the work distance of the applied force, D is the calculated displacement from the simulation, and w is the width of the mirror plate or inner frame (Fig. 3(c)). The estimated torsional force

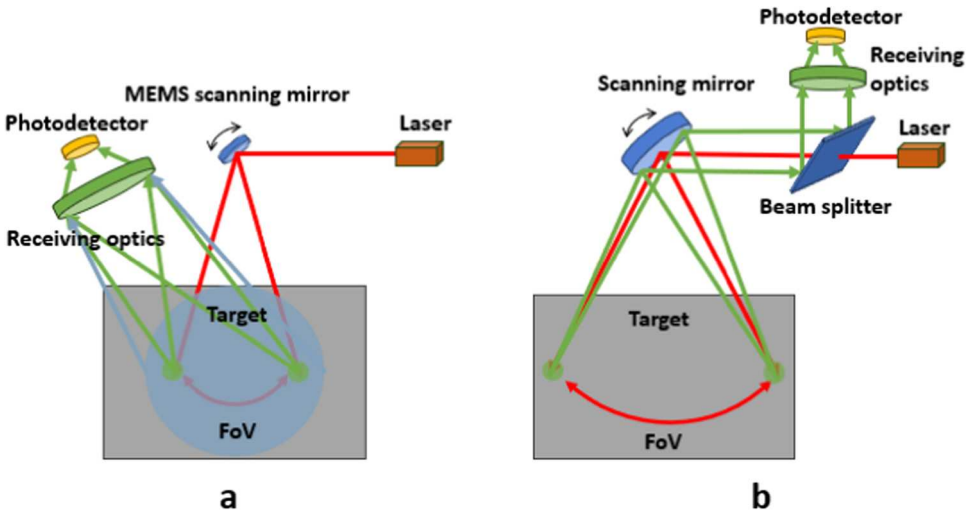

Fig. 1. (a) MEMS mirror-based scanning LiDAR system with non-coaxial architecture (b) Large mirror-based scanning LiDAR system with coaxial architecture.

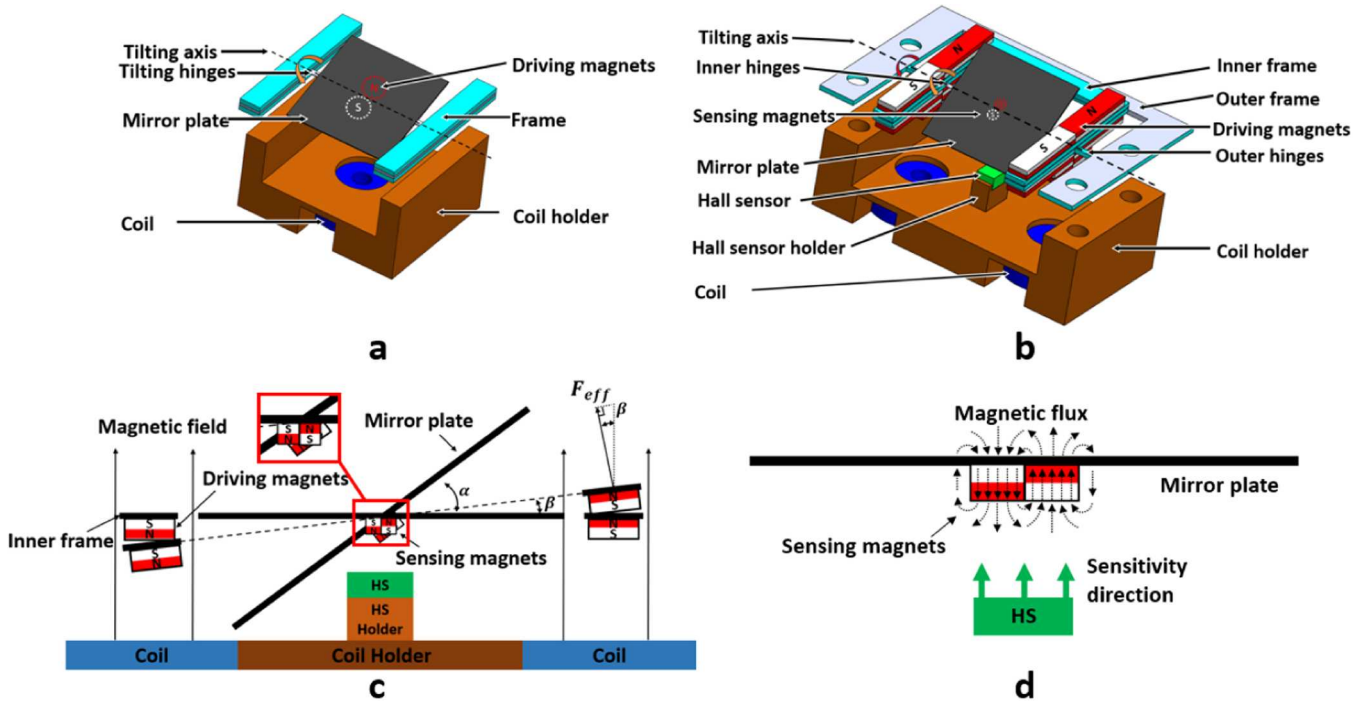

Fig. 2. Schematic design of the electromagnetic (a) direct-driving scanning mirror and (b) indirect-driving scanning mirror (c) Illustration of the tilting angle amplification through mechanical coupling (d) The representative magnetic flux of the sensing magnets and the position and sensitivity direction of the Hall sensor.

Table 1
The material properties of BoPET and acrylic hinges and other main design parameters.

BoPET hinge Young's modulus (E)	2.7 *GPa*
Acrylic hinge Young's modulus (E)	3.2 *GPa*
BoPET hinge Poisson ratio	0.38
Acrylic hinge Poisson ratio	0.35
BoPET hinges size ($l \times w \times t$)	$1.5 \times 0.75 \times 0.1$ mm^3
Acrylic hinges size ($l \times w \times t$)	$3 \times 0.75 \times 0.8$ mm^3
The mirror plate size ($l \times w \times t$)	$17 \times 17 \times 0.2$ mm^3
The overall inner frame size ($l \times w \times t$)	$27 \times 27 \times 1.7$ mm^3
The inner frame side width	3.5*mm*
Big driving magnet size ($l \times w \times t$)	$13 \times 3 \times 1.6$ mm^3
Small driving magnet size ($l \times w \times t$)	$5 \times 3 \times 1.6$ mm^3
The mirror size ($l \times w \times t$)	$45 \times 33 \times 5$ mm^3
Hall sensor size ($l \times w \times t$)	$4 \times 3 \times 1.6$ mm^3
Sensing magnet size ($d \times h$)	1.6×0.8 mm^2
Magnet density	7.5 g/cm^3

constants of a single inner and outer hinge were 1.96×10^{-4} N/rad and 2.18×10^{-2} N/rad, respectively.

In this design, the mirror plate, the inner frame and the two hinges can be considered as a two-degree-of-freedom (2-DOF) mass-spring system with two moving masses and two springs. A 2-DOF mass-spring system has two different coupled resonance frequencies depending on whether two masses move in phase or out of phase. The mechanical amplification ratio is defined as the ratio between the tilting angle of the mirror plate (α) and that of the inner frame (β) at the same tilting frequency (Fig. 2(c)). At frequencies near the resonance, damping plays a dominant role in the tilting amplitude of the mirror plate and the inner frame. Viscous damping of both mirror plate and inner frame in air should be small. The inner frame encounters higher structural damping than the mirror plate from the anchor loss (between the fixed outer frame and the stiffer outer hinges) and the electromagnetic damping (between the driving coil and the DMs). As a result, the mechanical amplification ($\alpha > \beta$) can be realized when the resonance frequencies of the mirror plate and the inner frame are matched. Higher amplification

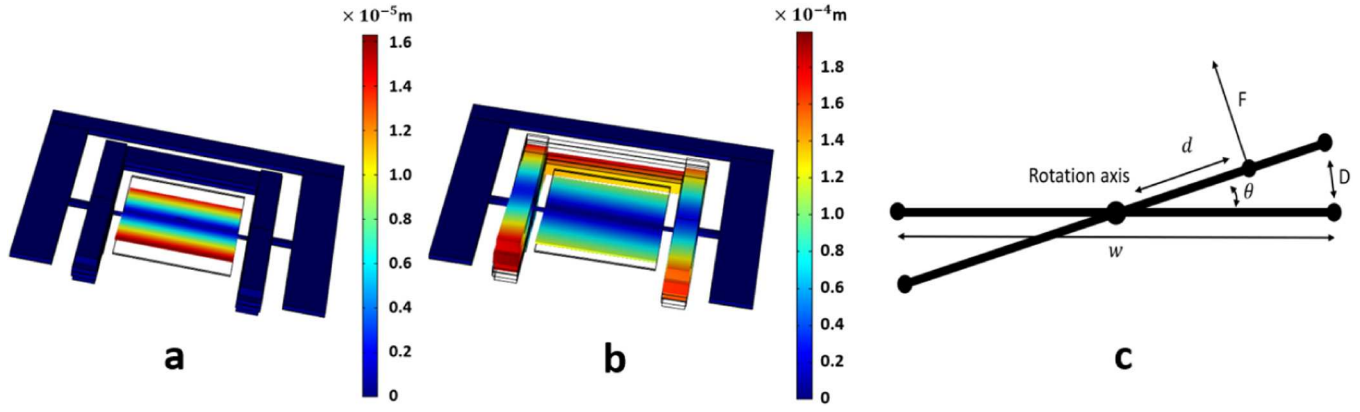

Fig. 3. Simulated linear displacement of (a) the mirror plate and (b) the inner frame under the applied normal loads (c) The schematic calculation diagram for the torsional force constant.

can be achieved by optimizing the mass moment ratio between the inner frame and the mirror plate, the force constants of the hinges, and their anchor design and bonding [25,29].

The calculated torsional force constants from COMSOL Multiphysics® were plugged into MATLAB to calculate the coupled resonance frequencies and the angular displacement responses of the mirror plate and the inner frame. The calculation was based on the equations of motion (EOM) of a 2-DOF system,

$$\begin{bmatrix} I_m & 0 \\ 0 & I_f \end{bmatrix}\begin{bmatrix} \ddot{\theta}_m \\ \ddot{\theta}_f \end{bmatrix} + \begin{bmatrix} C_m & 0 \\ 0 & C_f \end{bmatrix}\begin{bmatrix} \dot{\theta}_m \\ \dot{\theta}_f \end{bmatrix} + \begin{bmatrix} 2k_i & -2k_i \\ -2k_i & 2(k_i + k_o) \end{bmatrix}\begin{bmatrix} \theta_m \\ \theta_f \end{bmatrix} = \begin{bmatrix} 0 \\ M_{mag}\sin(\omega t) \end{bmatrix} \quad (2)$$

where I, C, k, $\ddot{\theta}$, $\dot{\theta}$, θ are the mass moment of inertia, the damping constant, the torsional force constant, the angular acceleration, the angular velocity, the angular displacement, the notation m, f,i and o are referred to the mirror plate, the inner frame, the inner hinge and the outer hinge, M_{mag} is the maximum amplitude of the applied torque on the magnets, ω is the angular frequency of the applied torque. Fig. 4(a) shows the calculated and normalized maximum angular displacement of the mirror plate and the inner frame vs. the frequency of the applied torque. The coupled resonance frequency was determined as the frequency where the angular displacement reaches maximum. The first coupled resonance frequency of the mirror plate and the inner frame were 54.4*Hz* and 53.8*Hz*, respectively. The second coupled resonance frequencies of the mirror plate and the inner frame were 65.3*Hz* and 65.7*Hz*, respectively. The maximal amplification ratio was 19.6 at the first coupled resonance frequency of the mirror plate. Coupled eigenfrequencies were also simulated by COMSOL Multiphysics® to verify the results. Fig. 4(b) and 4(c) show the first and second mode shapes of the scanning mirror. The simulated isolated and coupled resonance frequencies are listed in Table 2.

Previously, using a 1D Hall sensor with a single sensing magnet to monitor the tilting angle of the mirror plate was demonstrated [30]. However, it was limited to small tilting angles because it directly measured the magnetic field strength difference (instead of the relative direction) caused by the distance change between the Hall sensor and the sensing magnet. When the tilting angle is large (leading to several millimeter displacement of the sensing magnet), the sensing magnet will move either too close (causing saturation) or too far (causing no signal) to the Hall sensor. Such limitations can be addressed by replacing the single sensing magnet with a pair of magnets with opposite polarity at the middle of the mirror plate to enable scan position sensing by monitoring the change of the magnetic field direction. A finite element simulation was also conducted with COMSOL Multiphysics® to show the magnetic flux of the pair of sensing magnets with respect to the detection direction (i.e., Z axis) of the Hall sensor. As shown in Fig. 5(a), the overall magnetic field strength is relatively uniform over the Hall sensor. When the mirror plate is at the rest position (i.e., $\theta = 0°$), the magnetic flux is almost perpendicular to the Z axis (indicated by the green arrow in Fig. 5) of the Hall sensor, which causes a low response of the Hall sensor. When the tilting angle of the mirror plate increases, the magnetic flux will be better aligned to the detection direction of the Hall sensor (Fig. 5(b)), which results in a higher response of the Hall sensor. As a result, the scan position sensing could be achieved even at large tilting angles.

4. Fabrication and assembly

Fig. 6 illustrates the fabrication and assembly process of the electromagnetic indirect-driving scanning mirror. First, a 200-μm-thick aluminum-coated silicon wafer was diced into $17mm \times 17mm$ square pieces to serve as the mirror plate. The BoPET hinge layer was cut from a 100-μm-thick BoPET film with a CO_2 laser cutter. The acrylic hinge layer and two inner frames were laser cut out from a 0.8-*mm*-thick acrylic sheet. The silicon mirror plate, the BoPET hinge layer, the acrylic hinge layer, and the inner frame were aligned and bonded together with silicone adhesive (Momentive Performance Materials RTV108) (Fig. 6(a)). Second, four pairs of large driving magnets (B821, K&J Magnetics), two pairs of small driving magnets (B321, K&J Magnetics), and one pair of sensing magnets (D101-N52, K&J Magnetics) were aligned and bonded together with silicone adhesive onto the fabricated hinge layer (Fig. 6 (b)). Third, a 1D Hall sensor (SS49E, Honeywell Sensing and Productivity Solutions) was fixed onto the 3D printed holder, which was bonded onto the 3D printed coil holder with silicone adhesive. The assembled top mirror structure was mounted on the coil holder. Two coil-type electromagnets (YJ-15/5, YJ Electric Store) were inserted inside the coil holder to complete the fabrication and assembly (Fig. 6(c)). Fig. 7 shows the top and side view of the fabricated prototype of the electromagnetic indirect-driving scanning mirror.

5. Characterization

A double-laser tracing method was used to characterize the scanning performance (Fig. 8). The scanning mirror was fixed on a 3D printed backboard at 45° towards a reading screen. An additional small reflector was attached onto the inner frame. Two collimated CW laser beams (red and green) were shot onto the center of the mirror plate and the small

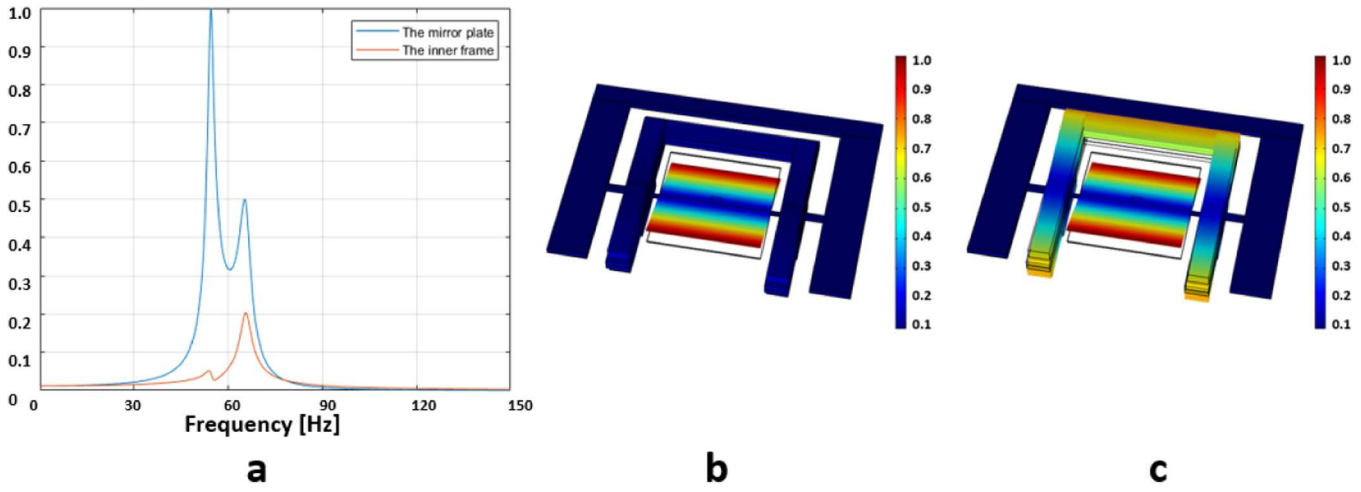

Fig. 4. (a) The calculated and normalized maximum angular displacements of the mirror plate and the inner frame at different driving frequencies. (b) The first and (c) the second mode shape of the scanning mirror.

Table 2
Resonance frequency simulation results.

	Simulated isolated eigen-frequencies from COMSOL	Simulated first coupled resonance frequencies from MATLAB/COMSOL	Simulated second coupled resonance frequencies from MATLAB/COMSOL
The mirror plate	56.1*Hz*	54.4*Hz*/54.6*Hz*	65.3*Hz*/66.4 *Hz*
The inner frame	65.7*Hz*	53.8*Hz*/54.6*Hz*	65.7*Hz*/66.4 *Hz*

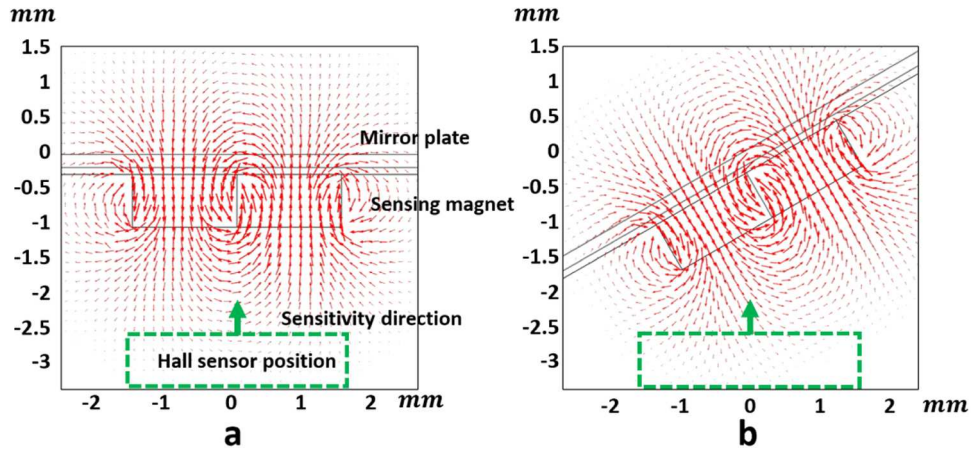

Fig. 5. (a) The simulated magnetic flux density of (a) a pair of sensing magnets without tilting and (b) a pair of sensing magnets tilted to a large angle.

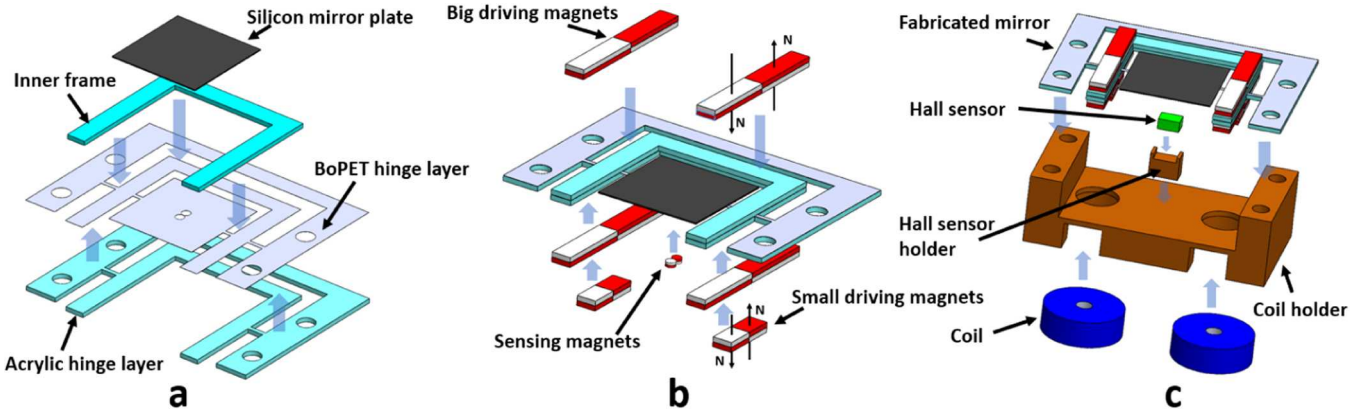

Fig. 6. Fabrication and assembly of the electromagnetic indirect-driving scanning mirror.

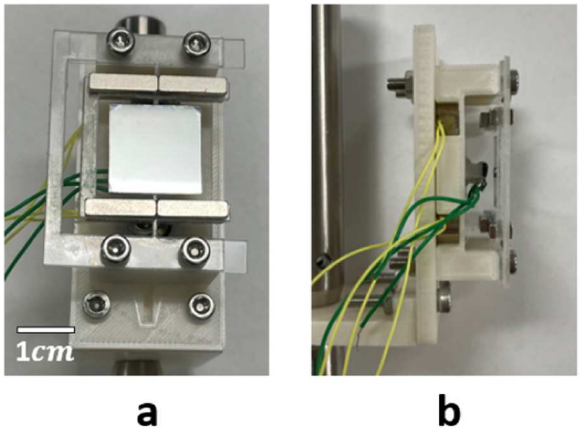

Fig. 7. (a)The top and (b) side view of the fabricated prototype scanning mirror.

reflector on the inner frame at an incident angle of 45°, respectively. The incident laser beams were reflected onto the reading screen at certain distances away. The optical tilting angles of the mirror plate and inner frame were calculated from the length of the red and green laser traces and their travel distances on the reading screen.

The isolated resonance frequencies of the mirror plate and the inner frame were characterized to ensure their resonance frequencies match with each other. The amplitude of the AC driving voltage for each coil was set to 2*Vpp* (corresponding to the driving current of 13.7 *mApp* and the power consumption of 3.4 *mW*). The frequency of the AC driving voltage was swept from 1*Hz* to 200*Hz* to reveal the resonance frequencies. Both inner frame and outer frame were fixed for testing the mirror plate by using another temporary coil to actuate the sensing magnets, while both mirror plate and outer frame were fixed for testing the inner frame by using the two assembled coils to actuate the driving magnets. The results were 57*Hz* and 61*Hz*, respectively. The coupled resonance frequencies of the mirror plate and the inner frame were also characterized. Fig. 9 shows the optical tilting angles of the mirror plate and the inner frame vs. frequency, respectively. The first coupled

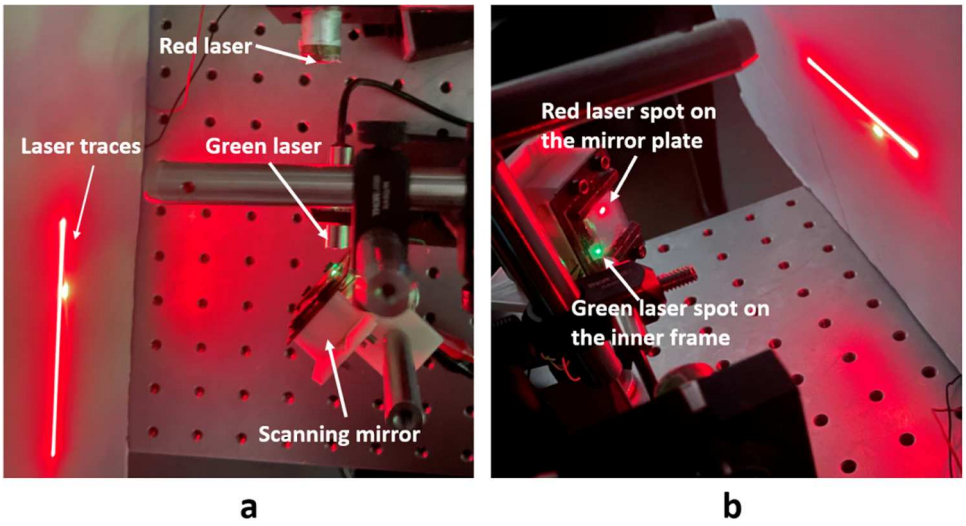

Fig. 8. (a) Top view and (b) side view of the double-laser tracing setup.

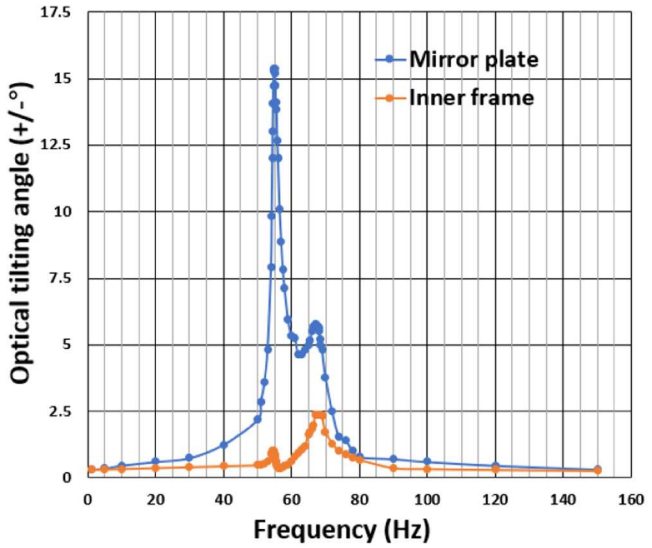

Fig. 9. Characterization of coupled resonance frequencies of the mirror plate and the inner frame.

resonance frequencies of the mirror plate and the inner frame were determined to be 54.9*Hz* and 54.5*Hz*, respectively. The second coupled resonance frequencies of the mirror plate and the inner frame were determined to be 67*Hz* and 67.6*Hz*, respectively. The actual maximum amplification ratio and quality factor at the first coupled resonance frequency of the mirror plate were estimated to be 15.0 and 14.4, respectively. Table 3 summarizes the actual resonance frequencies, which match well with the simulation results.

The AC driving response of the mirror plate and the inner frame was also tested. The frequency of the AC driving voltage was set at the first coupled resonance frequency of the mirror plate. The amplitude of the AC driving voltage for each coil was increased from 0*Vpp* to 13 *Vpp*. Based on the resistance (~146 Ω), the driving current and power consumption were calculated to be 89 *mApp* and 145 *mW*, respectively. The magnetic field output from the coil was estimated to be 4.55 mT from the measurement with a Gauss meter. The test was repeated three times. Fig. 10 shows the optical tilting angles of the mirror plate and inner frame vs. the amplitude of the AC driving voltage. The optical tilting angle of the mirror plate could reach a ±60 °, corresponding to an FoV of 120 °, which is larger than those of electromagnetic direct-driving scanning mirrors [14–17,31–36,44]. The viscous damping and its variation on the mirror plate are small at small tilting angles. Therefore, both the linearity and repeatability of tilting angle vs. the AC driving voltage are excellent at small tilting angles. However, the viscous damping and its variation increases rapidly with the tilting angle, which results in a slower increase rate of the tilting angle especially at larger tilting angles. The increase in the variation of the viscosity damping also reflects itself in the increase of the deviation of the tilting angle.

The Hall scan position sensor was characterized for its linearity and repeatability. The input voltage of the Hall sensor was set to $4V_{DC}$. The output of the Hall sensor was monitored with an oscilloscope. The optical tilting angle of the mirror plate (φ) and the corresponding output

Table 3
Actual resonance frequencies.

	Isolated resonance frequencies	First coupled resonance frequencies	Second coupled resonance frequencies
Mirror plate	57*Hz*	54.9*Hz*	67*Hz*
Inner frame	61*Hz*	54.5 *Hz*	67.6 *Hz*

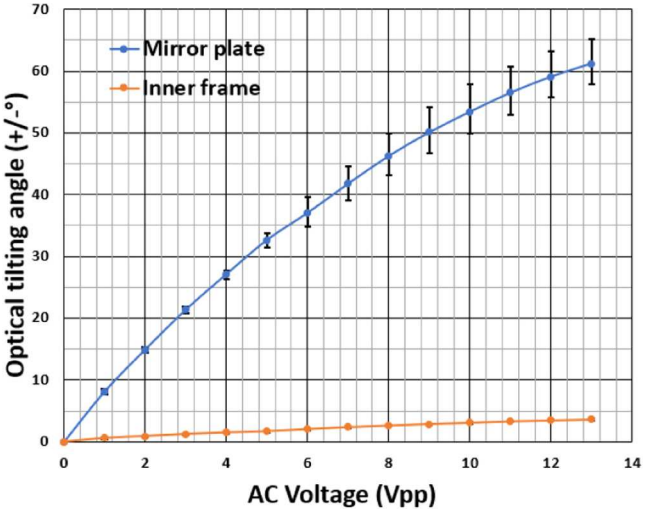

Fig. 10. The optical tilting angles of the mirror plate and the inner frame at the first coupled resonance frequency of the mirror plate.

voltage (*H*) of the Hall sensor at different AC driving voltage were recorded. The measurement was repeated three times. Fig. 11 shows three datasets of Hall sensor readings vs. the optical tilting angles of the mirror plate with a fitting line. The Hall sensor readings increased linearly with the optical scanning angle, which verifies the prediction of simulation. A small fluctuation was observed between datasets, which may be due to the vertical vibration of the mirror plate. If necessary, such fluctuation can be removed by using a calibration algorithm [37]. It should be mentioned that although the Hall scan position sensing has been applied in electromagnetic scanning mirrors with direct driving [30,38], complex signal processing has to be conducted to remove the interference from the driving coil and DMs to reveal the useful signals from the sensing magnets. With the indirect-driving mechanism, the driving magnets and coils are located far away from the mirror plate, the electromagnetic interference to the Hall scan position sensor is minimized and clean raw signals can be readily obtained.

A scanning angle limit testing was conducted to study the long-term operational stability of the electromagnetic indirect-driving scanning mirror. The scanning mirror was operated at different scanning angles for several hours. There was almost no change on the scanning performance when the scanning angle was below 120°. The resonance frequency started to drop slowly when the scanning mirror was driven beyond the scanning angle of 120° due to the excessive torsion of the hinges. More specifically, when the scanning mirror was operated at the scanning angle of 130°, it took about 15 min for the resonance frequency dropped from around 54 *Hz* to 50 *Hz*. So, the long-term operational stability of the scanning mirror is good as long as the scanning angle does not exceed a threshold value. Table 4 summarizes and compares similar works that have demonstrated scanning mirrors with large aperture. Compared with them, the electromagnetic indirect-driving scanning mirror achieved the largest FoV even though with relatively low resonance frequency. For real autonomous driving applications, the scanning angle (or FoV) would be the most critical specification to evaluate the scanning mirror's performance. For the resonance frequency, a resonance frequency of 10 s of Hz (corresponding to 2× frame rate) should be high enough for ordinary driving. A higher resonance frequency will result in sparser data points within each imaging frame and therefore lower imaging quality.

6. LiDAR imaging experiment

A prototype coaxial scanning LiDAR based on the electromagnetic indirect-driving scanning mirror was built to demonstrate the scanning and imaging capability (Fig. 12). It consists of an optical transceiver module, a fixed optics module, and the electromagnetic indirect-driving scanning mirror. The optical transceiver module has an infrared laser diode (905 nm with 20 kHz pulse repetition frequency), a photodetector (SF30/D, Lightware) with a convex receiving lens, and a microcontroller (MC). In the fixed optics module, a redirection mirror and a reception mirror (with a 6-mm wide hole) were placed with 45° facing down in a 3D printed enclosure. Both mirrors were made of 500-*um*-thick aluminum-coated silicon wafer. The fixed optics module was mounted right above the optical transceiver module to allow the reflected laser to go through the middle of the hole. The scanning mirror was held at 45° facing out in the front of the fixed optics module at a distance of ~4 cm to provide proper scanning range and reception sensitivity. A two-channel function generator (FG) was used to drive the scanning mirror and provide power for the Hall sensor. The output of the Hall sensor was monitored by an oscilloscope (OS). The infrared laser and photodetector were controlled by a PC through the microcontroller. Microcontroller also converted the *ToF* (time-of-flight) into the distance information. A data acquisition (DAQ) card (PCI 6251, National Instruments) was used to record the driving signal of the scanning mirror and both response signals of the Hall sensor and microcontroller. The microcontroller and the DAQ card were synchronized by the same trigger signal from the PC to register the corresponding spatial location of each laser pulse (Fig. 12 (c)).

Three white boards were individually mounted on three pipes as imaging targets (Fig. 13(a)). The electromagnetic indirect-driving scanning mirror was driven with a 50-*Hz* sinusoidal signal (corresponding to a 100-*Hz* effective imaging frame rate) with an amplitude of 10 *Vpp* (to match with the new resonance frequency of the scanning mirror). When the Hall sensor signal displayed on the OS was stable, the driving signal of the scanning mirror and the response signals of the Hall sensor and the microcontroller were recorded. The calculated distance from the microcontroller was plotted vs. the scanning time (Fig. 13(b)). The actual angular position of the scanning mirror plate was calculated from the output signal of the Hall sensor based on the fitting line (Fig. 13 (c)), which indicates an FoV of 97 °. Based on the ratio between the pulse repetition rate (20k *Hz*) and the effective imaging frame rate (100 *Hz*), every back or forth scanning cycle of the scanning mirror consists of 200 uniformly distributed laser pulses over the scanning time. The lowest angular resolution was estimated as 0.76° by the largest angular displacement difference ($\Delta\theta$) between the two laser pulses around the

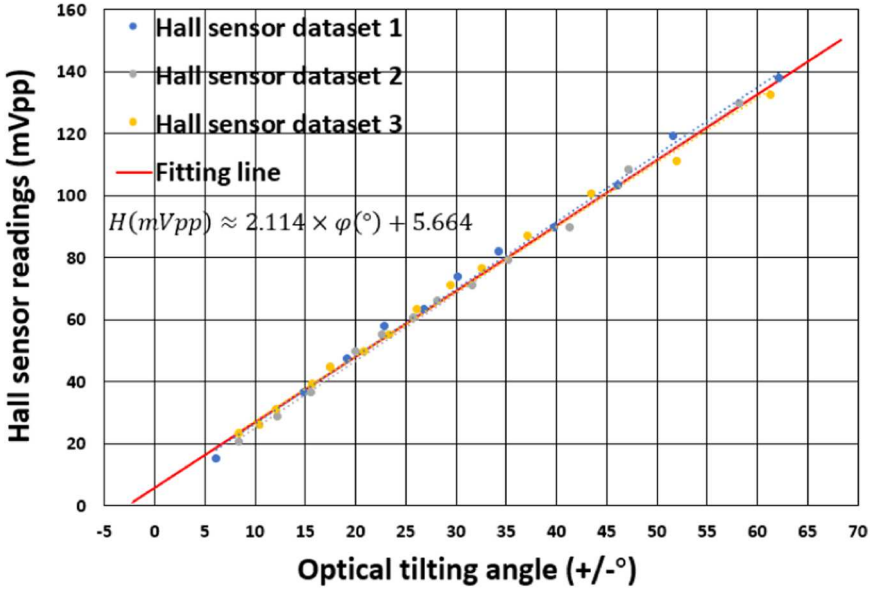

Fig. 11. Hall sensor readings versus optical tilting angles.

Table 4
The comparison of scanning mirrors with large aperture.

	Mirror Plate Dimension	Resonance Frequency	Optical FoV	Driving Signal Amplitude/Power	Mirror Position Sensor
This work	17 × 17 mm^2	54 Hz	120°	178 mApp/290 mW	Hall Sensor
[39]	25 × 50 mm^2	42–49 Hz	66.8°	16Vpp/400 mW	PSD
[40]	D=12 mm	1240 Hz	26°	250 mA/NA	PSD
[41]	10 × 10 mm^2	234 Hz	10°	7 V/NA	No
[42]	D = 20 mm	610 Hz	7.2°	120 V/NA	No
[43]	8 × 8 mm^2	60 Hz	90°	70 mA rms/210 mW	No

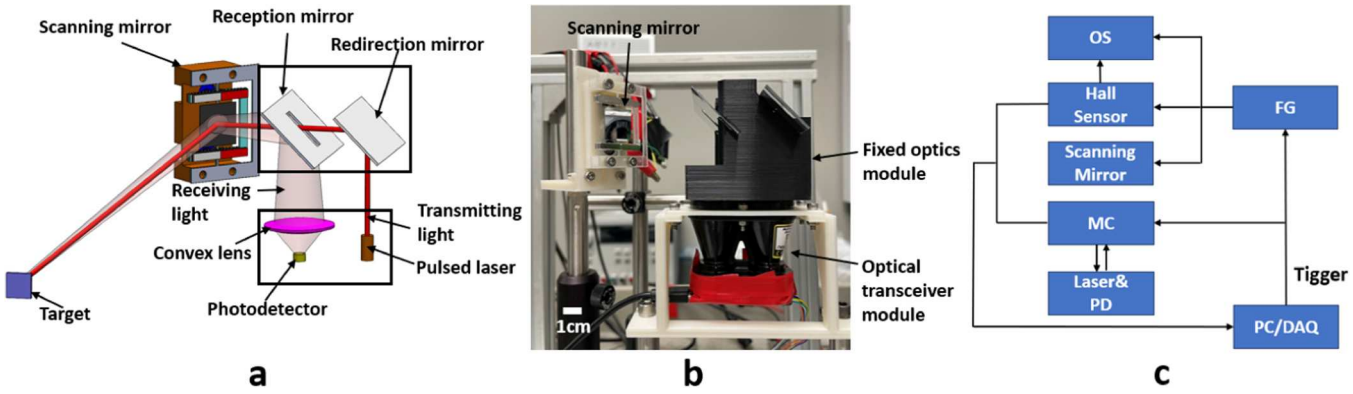

Fig. 12. (a) Schematic design, (b) real setup and (c) signal flow of the coaxial scanning LiDAR system.

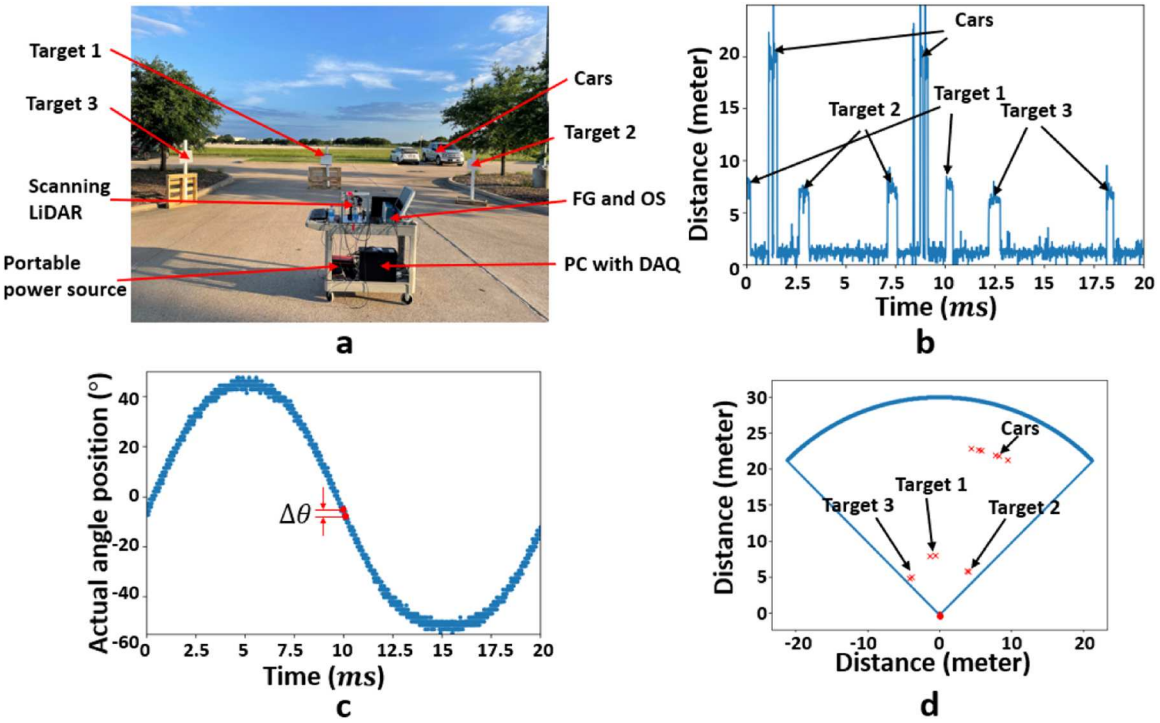

Fig. 13. (a) Photo of the field test setup (b) Distance of the targets acquired within one scanning cycle (c) Angular position of the mirror plate within one scanning cycle (d) Reconstructed 2D LiDAR image.

center of the FoV. The angular resolution increased when the scanning mirror scanned towards the two sides. A 2D image was reconstructed based on the average distance of each peak signal and the actual angular position of the scanning mirror (Fig. 13(d)). It shows that the reconstructed targets 1, 2, and 3 were in the range of 7.7–8.2 m, 6.7–7.3 m, and 5.8–6.3 m, respectively. The measured distances are in good agreement with their actual distances measured by a point LiDAR (8.03 m, 6.96 m, 6.13 m with statistical errors are around 4.1 %, 4.9 %, and 5.4 %). In addition to three designed targets, cars at ~22 m away could also be detected and mapped correctly. These results prove the

concept of the prototype coaxial scanning LiDAR using the electromagnetic indirect-driving scanning mirror with Hall position sensing.

7. Conclusion

In conclusion, a new electromagnetic indirect-driving scanning mirror was investigated to enable coaxial LiDAR designs combining the benefits of MEMS mirror- and rotational motor-based approaches.To validate the concept, a prototype scanning mirror with an enlarged mirror plate was designed, fabricated, and tested. 2D LiDAR imaging was also demonstrated with a coaxial setup based on the prototype scanning mirror. With the indirect-driving mechanism, the additional mass contributed by the electromagnetic actuator components can be removed from the mirror plate, which alllows softer hinges to be used to achieve a larger torsion angle without reducing the resonance frequency. Also, large amplification of the tilt angle can be obtained by carefully matching the resonance frequencies of the actuator and mirror plate. Due to the gimbal design, there is still a trade-off between the maximal tilt angle and resonance frequency of the mirror plate. However, compared with direct driving, the indirect-driving mechanism can be more effective to deal with this trade-off and improve the overall beam steering performance (i.e. speed and FoV) of the scanning mirror even with a relatively large mirror plate. This provides a wider design space for selecting the right tilt angle and resonance frequency to meet beam steering needs for different LiDAR applications.

CRediT authorship contribution statement

Jun Zou: Writing – review & editing, Supervision, Methodology, Conceptualization. **Shuangliang Li:** Writing – original draft, Investigation. **Di Wang:** Investigation. **Dezhen Song:** Supervision, Methodology, Conceptualization.

Declaration of Competing Interest

The authors declare the following financial interests/personal relationships which may be considered as potential competing interests: Jun Zou reports financial support was provided by National Science Foundation. Jun Zou reports financial support was provided by National Institutes of Health. If there are other authors, they declare that they have no known competing financial interests or personal relationships that could have appeared to influence the work reported in this paper

Data Availability

No data was used for the research described in the article.

Acknowledgments

This work is supported in part by awards (NRI-1925037, CBET-2036134 and PFI-2329865) from the National Science Foundation and a grant (1R01EB031040–01A1) for the National Institutes of Health. Any opinions, findings, conclusions, or recommendations presented are those of the authors and do not necessarily reflect the views of the National Science Foundation and the National Institutes of Health.

References

[1] Ching-Pai Hsu, et al., A review and perspective on optical phased array for automotive LiDAR, IEEE J. Sel. Top. Quantum Electron. 27 (1) (2020) 1–16.
[2] Taehwan Kim, et al., A single-chip optical phased array in a wafer-scale silicon photonics/CMOS 3D-integration platform, IEEE J. Solid-State Circuits 54 (11) (2019) 3061–3074.
[3] Nathan Dostart, et al., Serpentine optical phased arrays for scalable integrated photonic lidar beam steering, Optica 7 (6) (2020) 726–733.
[4] Ryan Halterman, Michael Bruch, Velodyne HDL-64E LiDAR for Unmanned Surface Vehicle Obstacle Detection, in: Unmanned Systems Technology XII, Vol. 7692, SPIE, 2010.
[5] Thinal Raj, et al., A survey on LiDAR scanning mechanisms, Electronics 9 (5) (2020) 741.
[6] Dingkang Wang, Connor Watkins, Huikai Xie, MEMS mirrors for LiDAR: a review, Micromachines 11 (5) (2020) 456.
[7] Dingkang Wang, et al., A low-voltage, low-current, digital-driven MEMS mirror for low-power LiDAR, IEEE Sens. Lett. 4 (8) (2020) 1–4.
[8] Dingkang Wang, Sanjeev J. Koppal, Huikai Xie, A monolithic forward-view MEMS laser scanner with decoupled raster scanning and enlarged scanning angle for micro LiDAR applications, J. Micro Syst. 29 (5) (2020) 996–1001.
[9] Fabian Schwarz, et al., Resonant 1D MEMS Mirror with A Total Optical Scan Angle of 180° for Automotive LiDAR, in: MOEMS and Miniaturized Systems XIX, Vol. 11293, SPIE, 2020.
[10] Dingkang Wang, et al., A miniature LiDAR with a detached MEMS scanner for micro-robotics, IEEE Sens. J. 21 (19) (2021) 21941–21946.
[11] Y. Chen, D. Wang, L. Thomas, K. Dantu, S.J. Koppal, Design of an adaptive lightweight LiDAR to decouple robot-camera geometry, IEEE Trans. Robot. (2024).
[12] F. Pittaluga, Z. Tasneem, J. Folden, B. Tilmon, A. Chakrabarti, S.J. Koppal, Towards a mems-Based Adaptive Lidar (November). In 2020 International Conference on 3D Vision (3DV), IEEE, 2020, pp. 1216–1226 (November).
[13] F. Xu, D. Qiao, C. Xia, X. Song, W. Zheng, Y. He, Q. Fan, A semi-coaxial MEMS LiDAR design with independently adjustable detection range and angular resolution, Sens. Actuators A Phys. 326 (2021) 112715.
[14] Xiaoyu Duan, et al., A two-axis water-immersible micro scanning mirror using hybrid polymer and elastomer hinges, Sens. Actuators A Phys. 312 (2020) 112108.
[15] Song Xu, Chih-Hsien Huang, Jun Zou, Microfabricated water-immersible scanning mirror with a small form factor for handheld ultrasound and photoacoustic microscopy, J. Micro/Nanolithogr. MEMS MOEMS 14 (3) (2015), 035004-035004.
[16] Sehui Kim, et al., Two-axis polydimethylsiloxane-based electromagnetic microelectromechanical system scanning mirror for optical coherence tomography, J. Biomed. Opt. 21 (10) (2016), 106001-106001.
[17] S. Li, Z. Dong, P. Song, J. Zou, A water-immersible scanning mirror with hybrid polymer and elastomer hinges for high-speed and wide-field 3D ultrasound imaging, Sens. Actuators A Phys. 367 (2024) 115032.
[18] K. Meinel, C. Stoeckel, M. Melzer, S. Zimmermann, R. Forke, K. Hiller, T. Otto, Piezoelectric scanning micromirror with built-in sensors based on thin film aluminum nitride, IEEE Sens. J. 21 (8) (2020) 9682–9689.
[19] H.C. Cheng, S.C. Liu, C.C. Hsu, H.Y. Lin, F. Shih, M. Wu, W. Fang, On the design of piezoelectric MEMS scanning mirror for large reflection area and wide scan angle, Sens. Actuators A Phys. 349 (2023) 114010.
[20] F. Schwarz, F. Senger, J. Albers, P. Malaurie, C. Janicke, L. Pohl, U. Hofmann, Resonant 1D MEMS Mirror with A Total Optical Scan Angle of 180° for Automotive LiDAR, in: In MOEMS and Miniaturized Systems XIX, Vol. 11293, SPIE, 2020, pp. 46–62.
[21] L. Pohl, F. Schwarz, P. Blicharski, C. Janicke, O. Petrak, T. von Wantoch, U. Hofmann, Wide angle LiDAR Demonstrator Based on A Resonantly Operated 1D MEMS Mirror Capable of Scanning 180, in: In MOEMS and Miniaturized Systems XX, Vol. 11697, SPIE, 2021, March, pp. 89–105.
[22] Arda D. Yalcinkaya, et al., Two-axis electromagnetic microscanner for high resolution displays, J. Micro Syst. 15 (4) (2006) 786–794.
[23] M. Yoda, et al., A MEMS 1D optical scanner for laser projection display using self-assembled vertical combs and scan-angle magnifying mechanism, in: The 13th International Conference on Solid-State Sensors, Actuators and Microsystems, 2005, Digest of Technical Papers. TRANSDUCERS'05. Vol. 1. IEEE, 2005.
[24] A.R. Cho, A. Han, S. Ju, H. Jeong, J.H. Park, I. Kim, C.H. Ji, Electromagnetic biaxial microscanner with mechanical amplification at resonance, Opt. Express 23 (13) (2015) 16792–16802.
[25] A. Arslan, D. Brown, W.O. Davis, S. Holmstrom, S.K. Gokce, H. Urey, Comb-actuated resonant torsional microscanner with mechanical amplification, J. Micro Syst. 19 (4) (2010) 936–943.
[26] Andrew C.-L. Hung, et al., An electrostatically driven 2D micro-scanning mirror with capacitive sensing for projection display, Sens. Actuators A Phys. 222 (2015) 122–129.
[27] Jan Grahmann, et al., Integrated Piezoresistive Position Detection for Electrostatic Driven Micro Scanning Mirrors, in: MOEMS and Miniaturized Systems X, Vol. 7930, SPIE, 2011.
[28] Behrad Ghazinouri, Siyuan He, Trevor S. Tai, A position sensing method for 2D scanning mirrors, J. Micromech. Microeng. 32 (4) (2022) 045007.
[29] William Thomson, Theory of vibration with applications, CrC Press, 2018.
[30] X. Duan, D. Song, J. Zou, Steering co-centered and co-directional optical and acoustic beams with a water-immersible MEMS scanning mirror for underwater ranging and communication. In 2019 International Conference on Robotics and Automation (ICRA), IEEE, 2019, May, pp. 6582–6587.
[31] Shuangliang Li, Xiaoyu Duan, Jun Zou, Micromachined two-axis water-immersible scanning mirror using torsional and bending hinges, J. Opt. Microsyst. 1 (4) (2021), 044001-044001.
[32] Song Xu, Shuangliang Li, Jun Zou, A micromachined water-immersible scanning mirror using BoPET hinges, Sens. Actuators A Phys. 298 (2019) 111564.
[33] Hakan Urey, Sven Holmstrom, Arda D. Yalcinkaya, Electromagnetically actuated FR4 scanners, IEEE Photon. Technol. Lett. 20 (1) (2007) 30–32.
[34] Arda D. Yalcinkaya, Olgaç Ergeneman, Hakan Urey, Polymer magnetic scanners for bar code applications, Sens. Actuators A Phys. 135 (1) (2007) 236–243.
[35] Muyu Chen, et al., An Electromagnetically-Driven MEMS Micromirror for Laser Projection. 10th IEEE International Conference on Nano/Micro Engineered and Molecular Systems, IEEE, 2015.
[36] Fanya Li, et al., A large-size MEMS scanning mirror for speckle reduction application, Micromachines 8 (5) (2017) 140.

[37] D. Wang, X. Duan, S.H. Yeh, J. Zou, D. Song, Calibration system and algorithm design for a soft hinged micro scanning mirror with a triaxial hall effect sensor, IEEE Robot. Autom. Lett. (2024).
[38] Xiaoyu Duan, et al., Device Design and System Integration of a Two-Axis Water-immersible Micro Scanning Mirror (WIMSM) to Enable Dual-modal Optical and Acoustic Communication and Ranging for Underwater Vehicles, in: IEEE International Conference on Robotics and Automation (ICRA), 2021, IEEE, 2021.
[39] H. Zuo, S. He, Extra large aperture FPCB mirror based scanning LiDAR, IEEE/ASME Trans. Mechatron. *27* (1) (2021) 93–102.
[40] L. Ye, G. Zhang, Z. You, Large-aperture kHz operating frequency Ti-alloy based optical micro scanning mirror for LiDAR application, Micromachines 8 (4) (2017) 120.
[41] L. Wu, H. Xie, Large-Aperture, Rapid Scanning MEMS Micromirrors for Free-space Optical Communications. In 2009 IEEE/LEOS International Conference on Optical MEMS and Nanophotonics, IEEE, 2009, August, pp. 131–132.
[42] F. Senger, U. Hofmann, T. von Wantoch, C. Mallas, J. Janes, W. Benecke, A. Wetzig, Centimeter-Scale MEMS Scanning Mirrors for High Power Laser Application, in: In MOEMS and Miniaturized Systems XIV, Vol. 9375, SPIE, 2015, pp. 27–42.
[43] Bu Shin, Hyun, Dongho Oh, Seung-Yop Lee, A two-dimensional laser scanning mirror using motion-decoupling electromagnetic actuators, Sensors 13 (4) (2013) 4146–4156.

Shuangliang Li received the B.S. degree in microelectronics science and engineering from East China Normal University, Shanghai, China, in 2017. He is currently a Ph.D. student in the Department of Electrical Engineering of Texas A&M University. His current research is mainly focused on scanning mirror design and fabrication.

Di Wang received the B.E. degree in computer science from the Harbin Institute of Technology, Harbin, China, in 2017, and the master's degree from the Department of Computer Science and Engineering, Texas A&M University, College Station, TX, USA, in 2019. He is currently pursuing the Ph.D. degree in computer engineering with Texas A&M University, College Station, TX, USA. His research interests include robot perception, robot vision, sensor fusion, and localization.

Dezhen Song (Senior Member, IEEE) received the Ph.D. degree from the Department of Industrial Engineering and Operations Research, University of California, Berkeley, CA, USA, in 2004. He is a Professor and an Associate Department Head with the Department of Computer Science and Engineering, Texas A&M University, College Station, TX, USA. His research interests include networked robotics, distributed sensing, computer vision, surveillance, and stochastic modeling. Dr. Song received the Kayamori Best Paper Award of the 2005 IEEE International Conference on Robotics and Automation (with J. Yi and S. Ding) and the NSF Faculty Early Career Development (CAREER) Award in 2007. From 2008–2012, he was an Associate Editor for IEEE TRANSACTIONS ON ROBOTICS. From 2010–2014, he was an Associate Editor for IEEE TRANSACTIONS ON AUTOMATION SCIENCE AND ENGINEERING (T-ASE). He was a Senior Editor for IEEE ROBOTICS AND AUTOMATION LETTERS (RA-L), from 2017 to 2020. He is currently a senior editor for T-ASE.

Jun Zou received the Ph.D. degree in electrical engineering from the University of Illinois at Urbana-Champaign in 2002. In 2004, he joined the Department of Electrical and Computer Engineering, Texas A&M University, where he is currently a Full Professor and directs the Acoustic and Optical Microsystems Lab (AOML). His current research interests lie in the development of micro and nano opto-electro-mechanical devices and systems for biomedical imaging, robotics, and artificial intelligence applications. He is a Senior Member of the SPIE, a Senior Member of the IEEE, and a Member of OSA.